Article

Impact of Annealing on ZrO$_2$ Nanotubes for Photocatalytic Application

Safa Jemai [1,2], Lotfi Khezami [3], Kaouther Gueddana [1], Khaled Trabelsi [1], Anouar Hajjaji [1,*], Mosbah Amlouk [4], Bernabé Mari Soucase [2], Brahim Bessais [1] and Sami Rtimi [5,6,*]

1 Laboratoire de Photovoltaïque, Centre de Recherches et des Technologies de l'Energie, Technopole de Borj-Cédria, BP 95 Hammam-Lif, Tunis 2050, Tunisia
2 School of Design Engineering, Departamento de Fisica Aplicada, Universitat Politecnica de Valencia, Cami de Vera, 46022 Valencia, Spain
3 Department of Chemistry, Imam Mohammad Ibn Saud Islamic University (IMSIU), P.O. Box 5701, Riyadh 11432, Saudi Arabia
4 Laboratory of Nanomaterials, Nanotechnology and Energy (L2NE), Faculty of Sciences of Tunisia, El Manar University, 2092 Tunis, Tunisia
5 Ecole Polytechnique Fédérale de Lausanne (EPFL), EPFL-STI-IMX-LTP, Station 12, 1015 Lausanne, Switzerland
6 Global Institute for Water, Environment and Health, 1201 Geneva, Switzerland
* Correspondence: authors: physicshajjaji@gmail.com (A.H.); rtimi.sami@gmail.com (S.R.)

Abstract: This work aims to study the structural, optical, and photocatalytic properties of ZrO$_2$ nanotubes (NTs) that have been synthesized using the electrochemical anodization method. The structural and morphological characteristics of unannealed and annealed (400 °C, 500 °C, and 700 °C) ZrO$_2$ NTs were analyzed using X-ray diffraction (XRD), scanning electron microscopy (SEM), and transmission electron microscopy (TEM). Details of the structural and morphological results are depicted to clarify the effect of annealing temperature on the NTs. Furthermore, the reflectivity and photoluminescence of ZrO$_2$ NTs were found to depend on the annealing temperature. The resulting bandgap values were 3.1 eV for samples annealed at 400 °C and 3.4 eV for samples annealed at 550 and 700 °C. Thus, amorphous and annealed ZrO$_2$ NTs were tested in terms of their photocatalytic degradation of Black Amido (BA) dye. Samples annealed at 400 °C exhibited 85.4% BA degradation within 270 min compared to 77.5% for samples annealed at 550 °C and 70.2% for samples annealed at 700 °C. The anodized ZrO$_2$ NTs that were annealed at 400 °C showed the coexistence of tetragonal and monoclinic crystalline phases and exhibited the fastest photocatalytic performance against the BA dye. This photocatalytic behavior was correlated to the crystalline phase transformation and the structural defects seen in anodized ZrO$_2$.

Keywords: ZrO$_2$ nanotubes; anodization; Black Amido; photocatalysis; crystalline phases

1. Introduction

Wide-bandgap (bg) semiconductor materials have the limitation of visible light absorption since their bg mainly consists of O2p orbitals (E = 3 eV) [1]. They greatly enhance the efficiency of power conversion compared to their silicon (Si)-based counterparts. Wide-bg semiconductors allow the design of faster, shape-controlled, and highly reliable power devices. These capabilities make it possible to reduce weight, volume, and life-cycle costs. Today, wide-bandgap semiconductors are attracting much attention for their environmental applications, such as sensing, photocatalytic devices, solar conversion, and water splitting via bg engineering. Strain-induced bg engineering by means of tunable sizes and controlled shapes enhances the quantum confinement effect, allowing targeted applications [2].

Zirconium oxide (ZrO$_2$) is an inorganic ceramic material of great technological importance distinguished by its many useful properties; it is a refractory material with thermal

resistance [3], a high dielectric constant ($\varepsilon \approx 25$) [4], good mechanical behavior [5], chemical stability (except in acidic media) [6], is non-toxic [7], and has good biocompatibility [8]. Moreover, ZrO_2 stands out for its optical properties, essentially, its high refractive index [9] and large optical gap [6]. ZrO_2 is used in a wide range of applications, including energy storage (fuel cell electrolytes) [6], gas sensing (oxygen sensors) [10], heterogeneous catalysts [11], catalytic supports [12], jewelry [9], and as a biomaterial in medical implants [13]. Additionally, ZrO_2 is an n-type semiconductor material [14] with a wide bandgap. Two direct transitions characterize it; the tetragonal and the monoclinic gap energies differ slightly. The bandgap energy of the tetragonal phase of ZrO_2 is typically around 3.0–3.2 eV. This is lower than the monoclinic phase of ZrO_2, which has a bandgap energy of around 3.3–3.4 eV [15,16]. These characteristics imply a localized absorption spectrum in the ultraviolet range. It is a refractory material, possessing a relatively high refractive index in the interval of 2.15–2.18 eV [17], and greater transparency (about 42%) [18]. In 2004, for the first time, Tsuchiya and Schmuki succeeded in elaborating highly controlled self-organized zirconium oxide porous structures with pore sizes of about 10 nm. These structures were formed by anodizing zirconium (Zr) foil in an aqueous solution containing sulfuric acid (H_2SO_4) and a small amount of ammonium fluoride (NH_4F) [19,20]. The synthesis of ZrO_2 nanotubes by anodic oxidation really began with the work of Lee and Smyrl in 2005 [21]. They used a simple electrolyte, i.e., hydrogen fluoride (HF: H_2O). By applying a voltage of 10 V for 10 min, they obtained nanotubes with an amorphous structure of about 10 μm [9,22]. Tsuchiya et al. subsequently optimized the anodization conditions to develop the nanotubular structure of ZrO_2. They performed anodization in an electrolyte containing ammonium sulfate (($NH_4)_2SO_4$) and ammonium fluoride (NH_4F). They obtained a layer of self-organized vertical nanotubes with a diameter of 50 nm and a length of 17 μm [23]. In fact, when ZrO_2 nanotubes are anodized at temperatures lower than 400 °C, the resulting nanotubes have a smaller diameter, lower aspect ratio, and more amorphous surface structure than those anodized at higher temperatures. Yang et al. (2019) showed that with ZrO_2 anodized at 300 °C, the resulting NTs had a smaller diameter (35 nm) compared to NTs anodized at 500 °C, which had diameters of 80 nm [24]. The same research group showed that the aspect ratio of the NTs was also lower at lower anodizing temperatures, indicating a more truncated morphology with a more amorphous surface.

This work systematically studies the structural, morphological, optoelectronic, and photocatalytic properties of zirconia nanotubes (ZrO_2 NTs) elaborated via oxidative anodization. The morphology and the elemental composition of NTAs ZrO_2 films were investigated by transmission electron microscopy (TEM). The structural, morphological, and optical behaviors of the NTAs ZrO_2 films have been examined using X-ray diffraction (XRD), Scanning Electron Microscopy (SEM), and diffuse reflectivity. The effect of Pt content and different annealing temperatures on the photocatalytic activity of the ZrO_2 NTs was studied by employing Black Amido as a model dye for bioanalysis. This work is a step forward in the development of highly selective biosensors.

2. Results and Discussion

2.1. SEM, TEM, and EDX Studies

Figure 1 shows FE-SEM images of unannealed (as-grown) and annealed ZrO_2 NTs. One may notice that the annealing temperature modifies the diameter of the ZrO_2 NTs, together with their method of assembly. The NTs of as-grown zirconia are relatively dense, with no apparent cracks (Figure 1a). Some obvious cracks appeared at the surface of the ZrO_2 NTs at an annealing temperature of 400 °C (Figure 1b), whereas the surface was partially covered by loose solid matter. At an annealing temperature of 550 °C, the ZrO_2 NTs are gathered in densely packed large clusters. At an annealing temperature of 700 °C, the ZrO_2 NTs are detached into blocks. Therefore, the size and morphology of the ZrO_2 NTs depend on the annealing temperature. This morphological change is due to a structural modification displayed below via XRD analysis.
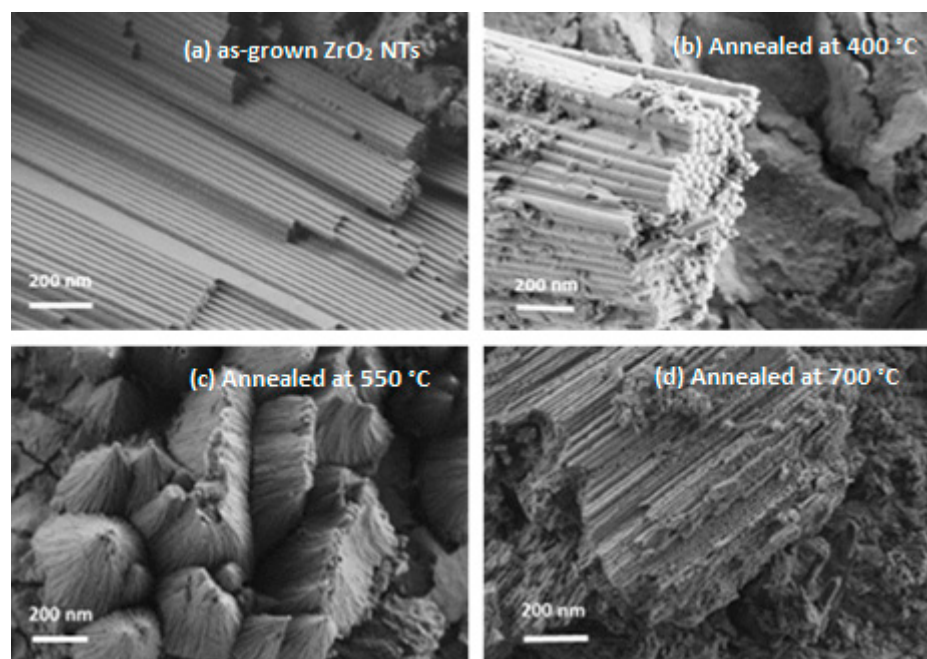
Figure 1. SEM images of (**a**) as-grown zirconia nanotubes and (**b**–**d**) after air annealing at different temperatures (400 °C, 550 °C, and 700 °C, respectively).

Figure 2 depicts the TEM images of two ZrO_2 NTs samples anodized under the same experimental conditions for 60 min at 40 V; no annealing was applied to the first sample (Figure 2a) while the second one was annealed at 550 °C (Figure 2b). The average external diameter was estimated to be 65 nm for both samples. Therefore, one can say that the annealing step does not affect the morphology of the nanotubes. Figure 2c shows the transparency of the anodized ZrO_2 NTs. This aspect will be further studied in the UV-vis spectroscopy section below. The EDX spectrum of the ZrO_2 NTs shown in Figure 3 reveals only the presence of Zr and O, confirming the formation of ZrO_x films and the absence of impurities. The copper content in this spectrum comes from the copper grid sample holder.
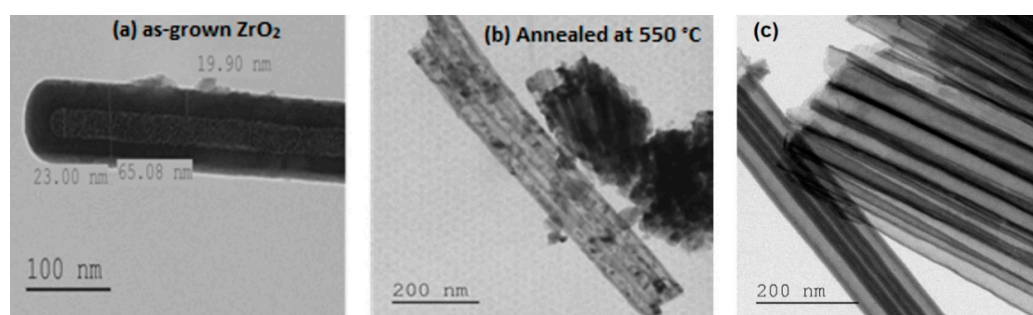

Figure 2. TEM images of the ZrO_2 nanotubes: (**a**) as-grown, (**b**) annealed at 550 °C in air, and (**c**) transparency of ZrO_2 nanotubes annealed at 550 °C.

Scheme 1 shows the different steps during the formation of anodized nanotubes. The first step consists of the formation of pores, which manifest as holes in the substrate. Then, the material starts to condense around the pores, forming circular islands. These latter islands elongate with the advancement of anodization time. Once they reach a certain length, the nanotubes start breaking down. The anodization step is responsible for the alignment and the crystallinity of the formed NTs.
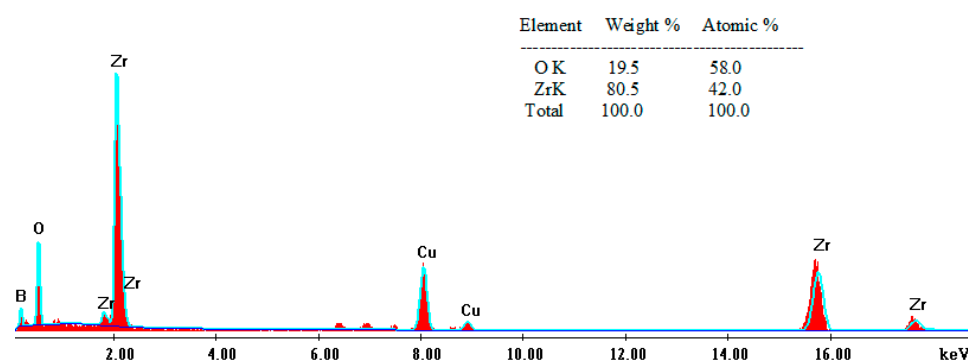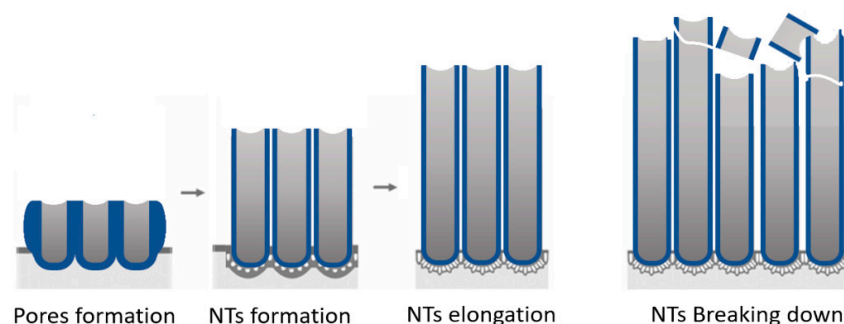
Figure 3. EDX spectrum of ZrO$_2$ NTs annealed at 550 °C.

Pores formation   NTs formation   NTs elongation   NTs Breaking down

Scheme 1. Steps in the formation of anodized ZrO$_2$ NTs.

2.2. X-ray Diffraction

The XRD patterns were recorded in the 2θ = 20–60° angle range for all ZrO$_2$ NT samples. Figure 4 shows the XRD patterns of as-grown and annealed ZrO$_2$ NTs. The appearance of a sole Zr peak in the unannealed samples indicates that the as-grown ZrO$_2$ is quasi-amorphous. Hence, all observed XRD peaks located at 2θ = 34.36°, 36.13°, 47.57°, 63.12°, and 73.20° correspond to the crystallographic orientations (002), (101), (102), (103), (004) of the hexagonal structure of metallic Zr (JCPDS card no. 00-005-0665).
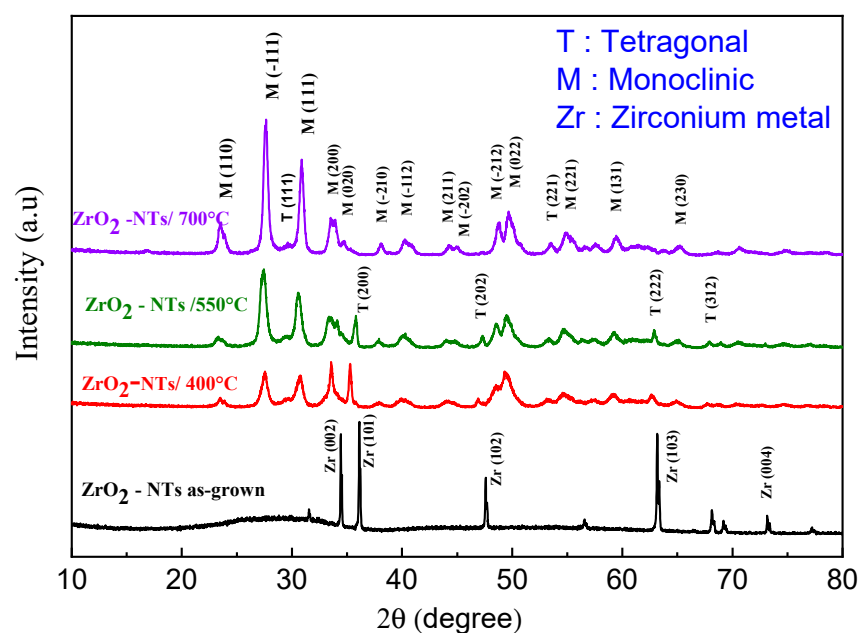

Figure 4. X-ray diffraction patterns of the as-grown and air-annealed ZrO$_2$ NTs at different temperatures (400 °C, 550 °C, and 700 °C).

After annealing in air at 400 °C and 550 °C, the newly appearing XRD peaks correspond to two crystalline phases: tetragonal (T-ZrO$_2$) and monoclinic (M-ZrO$_2$). At 700 °C, the tetragonal phase (T-ZrO$_2$) completely disappeared, and all diffraction peaks corresponded to the (M-ZrO$_2$) phase.

The XRD peaks of the annealed samples located at 2θ = 23.56°, 27.64°, 30.86°, 33.94°, 34.73°, 38.18°, 40.33°, 44.33°, 45.08°, 48.72°, 49.67°, 54.83°, 59.40°, and 65.22 correspond to the (110), (−111), (111), (200), (020), (−210), (−112), (211), (−202), (−212), (022), (221), (131), and (230) crystallographic orientations of the monoclinic ZrO$_2$ phase [JCPDS file: 37-1484], respectively. Conversely, the XRD peaks at 2θ = 29.54°, 35.29°, 47.32°, 53.44°, 62.86°, and 67.85 ° are attributed to the (111), (200), (202), (221), (222), (312) of the tetragonal ZrO$_2$ phase, respectively [JCPDS file: 17-0923]. Tetragonal zirconia forms at temperatures above 1170 °C; nevertheless, it can be stabilized at lower temperatures under the influence of internal compressive stresses. T-ZrO$_2$ can be formed by adding stabilizing elements or, probably, by decreasing the size of the crystallites. The tetragonal phase is thermodynamically stable if the crystallite size becomes smaller than a critical value, which is typically of the order of 20 to 30 nm [25–27]. The surface/interface energy of tetragonal zirconia crystallites would be lower than that of monoclinic crystallites. Indeed, Wang et al. [28] reported that tetragonal particle-shaped zirconia could be achieved at room temperature, with sizes beneath 40 nm. Similarly, Moulzolf et al. [29] and Yeh et al. [30] found that the ZrO$_2$ grain size does not exhibit a noticeable increase when heat-treated under 600 °C.

XRD patterns allowed the estimation of other parameters such as the interplanar distance, the full width at half-maximum (FWHM), and the crystalline sizes. The latter can be calculated using the Debye–Scherrer formula [31]:

$$D = (K\lambda / \beta \cos \theta) \tag{1}$$

where D is the crystalline size, λ is the X-ray incident beam wavelength, K is the Scherrer's constant (usually equal to 0.9), β is the width of the FWHM, and θ is the diffraction angle. All calculations were made using the (111) main peak of the monoclinic crystal phase.

The monoclinic phase content increases with annealing temperature, as shown in Figure 4. This, in turn, increases the mean crystallite size value, as illustrated in Table 1. These findings are in agreement with previous studies [32].

Table 1. Crystallite size as a function of the annealing temperature of ZrO$_2$ nanotubes.

Annealing Temperature (°C)	400	550	700
D (nm)	13.1	15	20.7

The lattice parameters were calculated using Bragg's law:

$$2d_{hkl} \sin \theta = n\lambda \tag{2}$$

where d_{hkl} is the inter-reticular distance, θ is the diffraction angle, n is an integer that denotes the diffraction order (n = 1), and λ is the wavelength of the Cukα X-ray line = 1.5406 Å. Let us consider the equations relating to the inter-reticular distance, d_{hkl}, and the unit cell parameters of the monoclinic (Equation (3)) and the tetragonal systems (Equation (4)) [33]:

$$d_{hkl} = \frac{1}{\sqrt{\frac{h^2}{a^2}\frac{1}{\sin \beta^2} + \frac{k^2}{b^2} + \frac{l^2}{c^2}\frac{1}{\sin \beta^2} - 2\frac{hl}{ac \sin \beta^2} \cos \beta}} \tag{3}$$

$$d_{hkl} = \frac{a}{\sqrt{h^2 + k^2 + l^2 \left(\frac{a}{c}\right)^2}} \tag{4}$$

From Bragg's law, one can determine the ZrO_2 lattice parameters corresponding to the tetragonal and monoclinic structures. We have summarized the calculated values in Table 2.

Table 2. The parameters of the monoclinic and tetragonal lattices of ZrO_2 NTs.

θ (rad)	Sin(θ)	(hkl)	D_{hkl} (Å)	Structure	Lattice Parameter (Å)
0.29	0.28	(200)	2.69		a = 5.5
0.30	0.29	(020)	2.58	Monoclinic	b = 5.2
0.43	0.41	(022)	1.84		c = 5.3
0.30	0.29	(200)	2.60	Tetragonal	a = b = 5.2
0.54	0.51	(222)	1.49		c = 5.1

Figure 5 shows the crystalline structures of the tetragonal and monoclinic phases and their combination. In the current case, the anodized ZrO_2 annealed at 400 °C showed the co-existence of both tetragonal and monoclinic phases. After annealing at 550 °C and 700 °C, the monoclinic phase was preponderant. The simulation in Figure 5 shows the coexistence of both phases but does not deal with their abundance from one to the other.
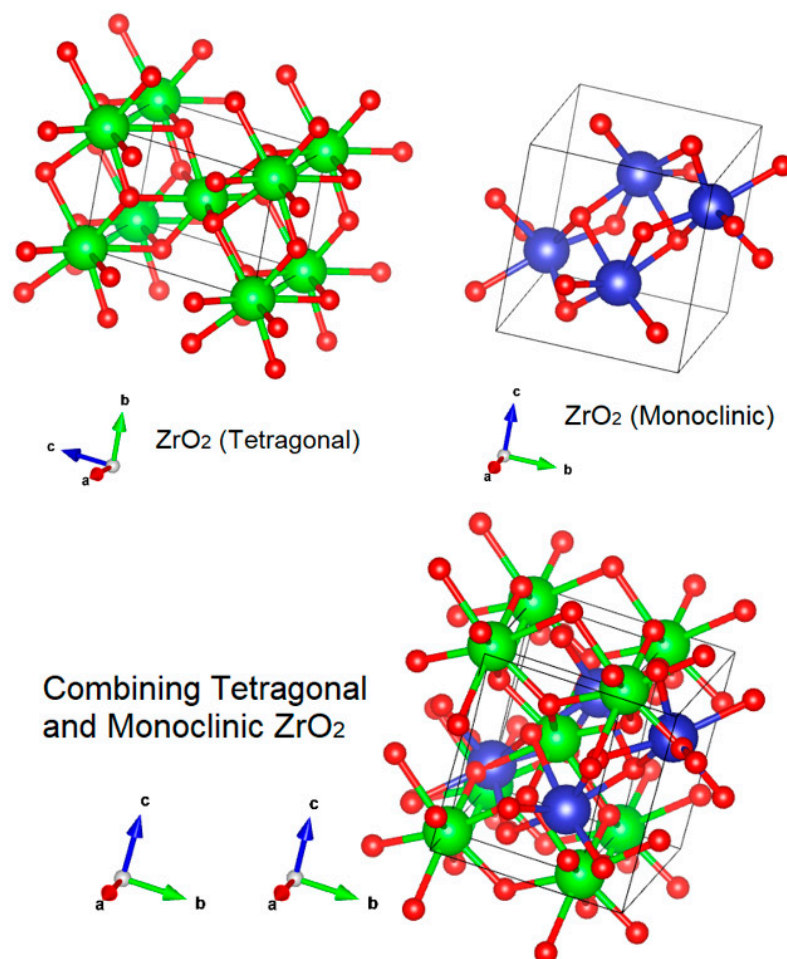

Figure 5. Simulation of the co-existence of tetragonal and monoclinic crystalline phases in ZrO_2 nanotubes annealed at 400 °C.

2.3. Optical Properties

Figure 6 shows the photoluminescence (PL) spectra of the as-prepared and annealed ZrO_2. The emission spectrum of the ZrO_2 NTs presents a broad band ranging from 380 nm

to 650 nm, with a peak centered at 485 nm for the annealed samples and a flat level for unannealed ZrO_2 NTs. The PL emission band of ZrO_2 could originate from impurities, intrinsic self-trapped excitons, and intrinsic defects such as singly ionized oxygen-vacancy defects (F^+ centers) and Zr^{3+} centers. The PL band can be deconvoluted into two bands located at 425 and 490 nm, as shown in Figure 7. Wang et al. [34] attribute these bands to F^+ centers and to $(F - F)^+$ singly ionized two-oxygen-vacancy-defect associations.
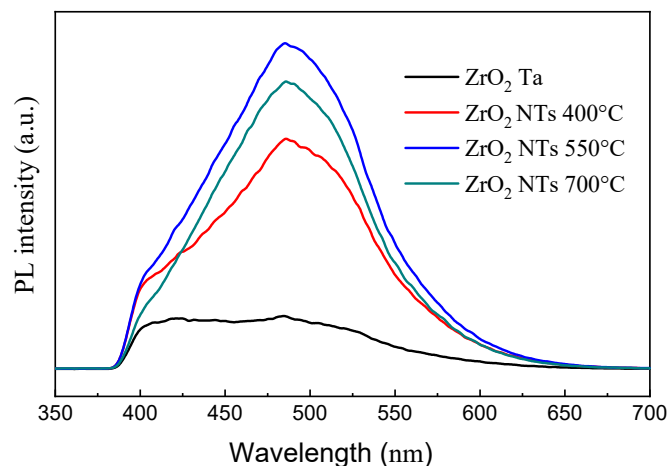

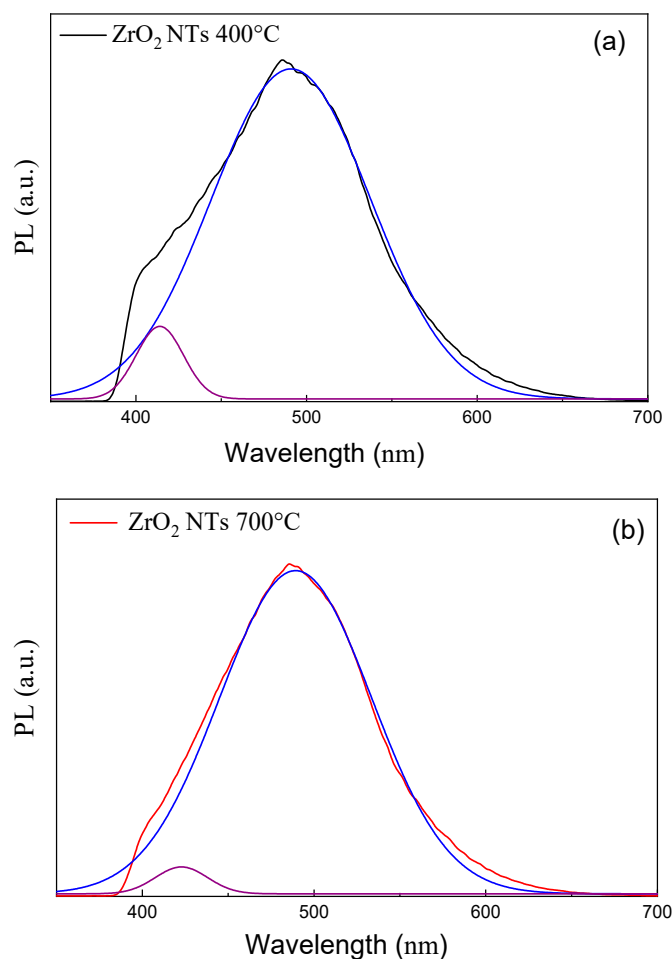**Figure 6.** Photoluminescence spectra of unannealed and annealed ZrO_2 NTs.

Figure 7. Deconvolution of the PL band spectrum of (**a**) 400 °C- and (**b**) 700 °C-annealed ZrO_2 NTs.

Salah et al. [35] attribute the broad peak centered on 490 nm to a self-activated luminescence originating from the asymmetry and unusual oxygen coordination of zirconium in monoclinic ZrO_2. The PL intensity increased with the annealing temperature, while the peak centered at 420 nm became smaller in comparison with the PL peak centered at 490 nm. This result can be explained by the increasing oxygen defects with the increase in annealing temperature and also by the crystallographic phase transformation from tetragonal to monoclinic ZrO_2, which, in turn, increases the probability of creating a two-oxygen-vacancy defect association.

Figure 8 depicts the diffuse reflectivity spectra of unannealed and annealed ZrO_2 nanotubes at different temperatures (400, 550, and 700 °C).
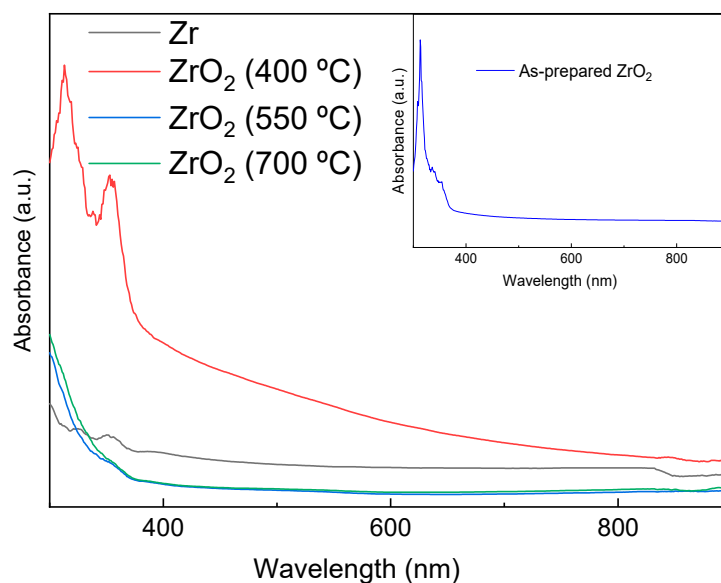

Figure 8. The light absorption spectra of unannealed ZrO_2 and annealed ZrO_2 NTs at different temperatures (400, 550, and 700 °C).

The Kubelka–Munk function, which associates the reflectance with the absorption and scattering coefficients, can be expressed by the following equation [36]:

$$F(R) = \frac{K}{S} = \frac{(1 - R)^2}{2R} \tag{5}$$

where K and S are the absorption and diffusion coefficients, respectively.

Zirconium dioxide is a direct bandgap semiconductor; its bandgap energy value (Eg) was graphically determined via Kubelka–Munk interpolation, using the variation of $(F(R) h\nu)^2$ as a function of the energy ($h\nu$). The corresponding curves are displayed in Figure 9.

From Figure 9, one can see that when the annealing temperature increases, the energy of the bandgap increases from 3.1 to 3.4 eV. This result can be explained by the co-existence of two phases in the ZrO_2 NTs, which probably add more defects, particularly at the interfacing sites between these crystalline phases. Then, increasing the annealing temperature led to an increase in tetragonal to monoclinic ZrO_2 crystalline phases, while enlarging the crystallite size. These results indicate the elimination of structural defects induced by the grain boundary, which leads to the elimination of additional levels in the bandgap, followed by an increase in the energy gap [37]. Mendez-Lopez et al. (2023) prepared ZrO_2 thin films that had been annealed at different temperatures and studied their transparency and hydrophilicity [38]. These authors concluded that the annealing temperature affected the structural properties of the tetragonal ZrO_2 as well as the hydrophilicity of the crystalline thin film. In our case, the annealing affected the size of the bandgap, which shifted from 3.1 to 3.4 eV, concomitant with the appearance of the monoclinic crystalline

phase. More work is needed in the future to correlate the crystalline phase of ZrO_2 with the material's chemistry. This aspect is beyond the scope of the current study. From another perspective, ZrO_2 NTs present a high level of hardness, which makes them suitable for sustainable applications.
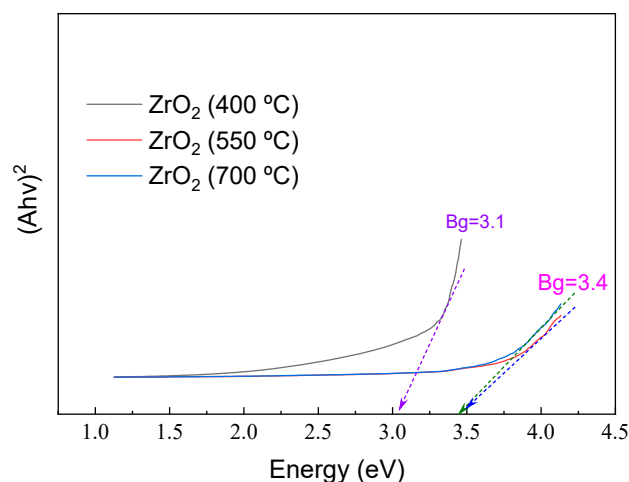

Figure 9. The Kubelka–Munk transformation of the diffuse reflectance spectrum for annealed ZrO_2 NTs.

2.4. Photocatalytic Degradation of Black Amido (BA) and the Stability of the Samples

It has been demonstrated elsewhere that the photocatalytic activity of pure monoclinic ZrO_2 is higher than that of tetragonal ZrO_2 under optimum identical conditions [39]. As shown above, the increase in the annealing temperature leads to the preponderance of the monoclinic phase at the expense of the tetragonal phase (Figure 4), which, in turn, can affect photocatalytic degradation activity.

To evaluate the effect of annealing temperatures on the photocatalytic efficiency of ZrO_2 NTs, we used a model organic pollutant (Black Amido—BA). The dye photodegradation rate using ZrO_2 NTs was estimated using the following equation [40]:

$$D(\%) = \frac{A_0 - A}{A_0} \times 100 \tag{6}$$

where A represents the absorbance of the dye solution, peaking at 618 nm after the photocatalytic experiments; A_0 represents the absorbance of the dye solution, peaking at 618 nm before the photocatalytic experiments. Figure 10a,b depicts the photocatalytic degradation of BA in the presence of unannealed and annealed ZrO_2 NTs.

Figure 10b shows the variation of the absorbance spectra of BA at 618 nm, as a function of UV light irradiation time for ZrO_2 NTs annealed at 400 °C. The decrease in photocatalytic efficiency as a function of the annealing temperature is related to the presence of the tetragonal phase. This, in turn, testifies to the existence of hydroxyl groups. It is worth mentioning that OH-radicals play a fundamental role in the formation and stabilization of the tetragonal phase in ZrO_2. They can act as a driving force for transforming the more common monoclinic phase into the tetragonal phase. In ZrO_2 NTs, hydroxyl radicals are principally confined within the tubes, which could affect the stability of the tetragonal phase. Moreover, the geometry of the NTs may affect the structure and stability of the tetragonal phase, compared to bulk ZrO_2. More research is needed to fully understand the correlation between the tetragonal crystalline phase, hydroxyl radicals' density, and the ZrO_2 NT structure.
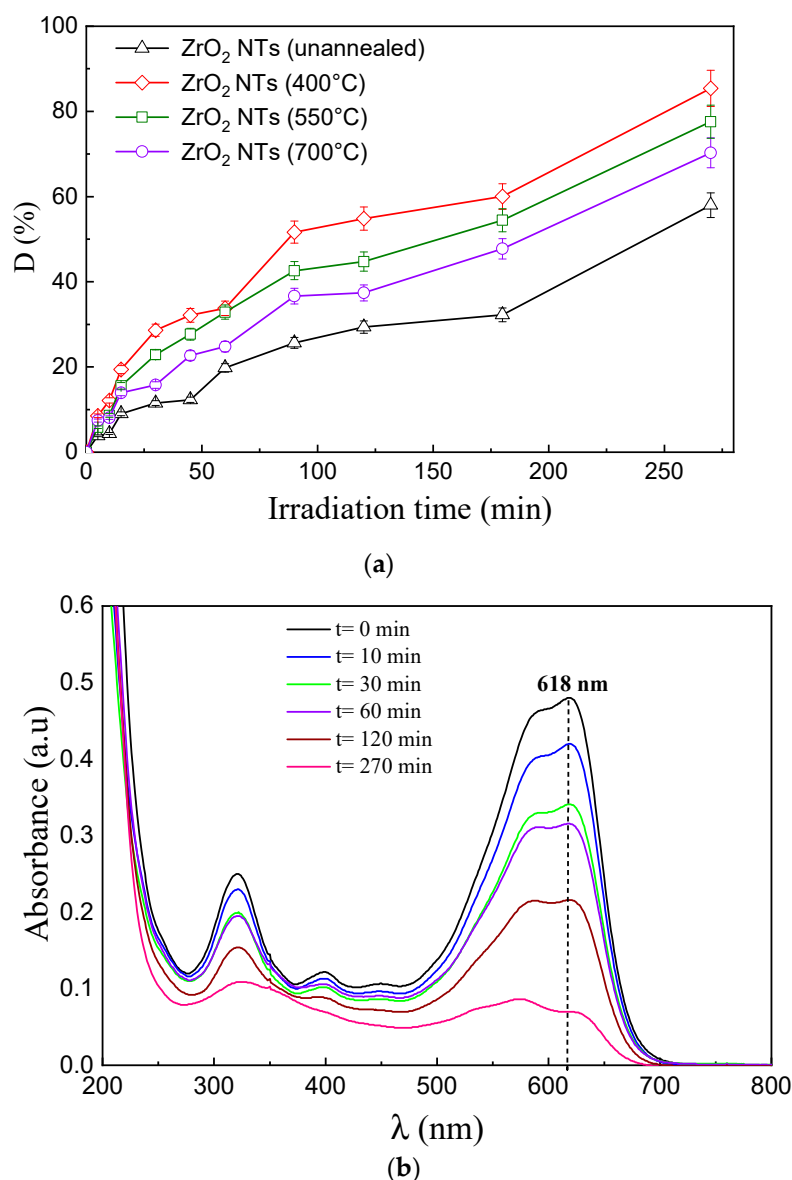
Figure 10. (**a**) The photocatalytic degradation of BA in the presence of unannealed and annealed ZrO$_2$ NTs (400, 550, and 700 °C) versus irradiation time. (**b**) Absorbance spectra illustrating Black Amido photo-degradation during UV light irradiation in the presence of ZrO$_2$ NTs (annealed at 400 °C).

The degradation of Black Amido by ZrO$_2$ NTs involves $^\bullet$OH radicals formed subsequently by the reaction of OH$^-$ ions with the photogenerated holes. From Table 3, significant degradation of BA can be seen, the best response of which is attributed to ZrO$_2$ NTs annealed at 400 °C, allowing 85% BA photodegradation. This phenomenon can be related to the breakdown of the azo groups, -N=N-, after the $^\bullet$OH radicals attack [40] into the formed intermediates.

Figure 11 displays a kinetic study of BA photodegradation as a function of time. The photocatalytic activity is expressed in terms of the apparent rate constant, *K*. This constant is obtained from the straight-line slope of ln(A_0/A) against the time plot (Equation (7)) [16,41]:

$$\ln\left(\frac{A_0}{A}\right) = Kt \tag{7}$$

Table 3. Photocatalytic performance of ZrO$_2$ NTs as a function of the annealing temperature.

Sample	Annealing Temperature (°C)	Degradation Rate (%)
	Unannealed	57.97
ZrO$_2$-NTs	400	85.41
	550	77.57
	700	70.28
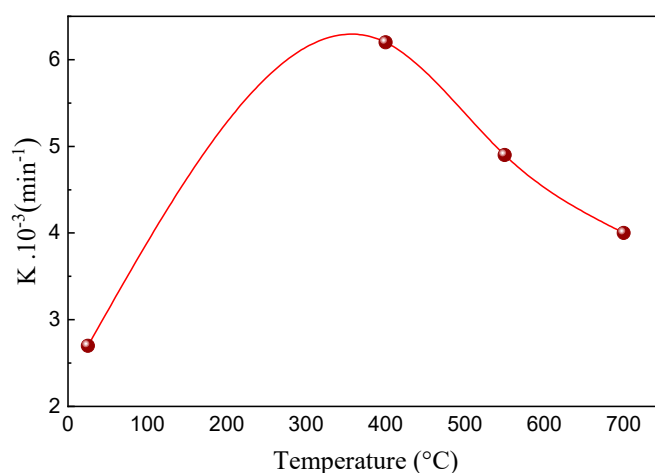
Figure 11. Kinetic study of ln (A_0/A) versus irradiation time in the presence of ZrO$_2$ NTs.

Perceptibly, the ZrO$_2$ NTs that were annealed at 400 °C show the highest photocatalytic performance, with the highest decolorization rate constant of $K = 6.2 \times 10^{-3}$ min^{-1}. Figure 11 shows that the samples annealed at 400 °C present the best photocatalytic performance. This result can be explained by the development of $^{\bullet}$OH and O$_2$$^{\bullet-}$ radicals, resulting from O$_2$ oxidation by an electron from the conduction band (CB) and the reduction of OH by the photogenerated holes at the valence band (VB), leading to BA degradation at the interface.

As was shown in the SEM images (Figure 1), at 400 °C we have well-ordered and outstanding ZrO$_2$ NTs. Upon raising the temperature to 550 °C, the NTs became clogged, doubtlessly eliminating their high specific surface area features. Further increasing the temperature to 700 °C led to the partial destruction of the NT structure. This explains the procured photocatalytic degradation results and the highest percentage for the 400 °C sample. In addition, the samples annealed at 550 °C and 700 °C exhibit higher diffuse reflectance than those at 400 °C, due to their exceedingly disordered structure. Moreover, these samples present broader gap energy, in contrast to the amorphous and 400 °C samples, which could be imputed to the evaporation of impurity dopants, such as F and C, etc. [16].

The PL spectra in Figure 6 showed that the 550 °C and 700 °C samples exhibited a higher PL intensity than those samples annealed at 400 °C. This can be attributed to the prevailing oxygen vacancies and the possibility of creating two-oxygen-vacancy defect association functions as a trap recombination center of e^{-}/h^{+} pairs, which explains their weak photocatalytic performance [42]. Basahel et al. (2018) assumed that tetragonal ZrO$_2$ exhibited the highest surface area [39]. However, the coexistence of two phases (monoclinic and tetragonal) in the samples annealed at 400 °C enhances the surface area compared to the pure monoclinic phase; yet, combined with its high photocatalytic activity, this leads to the improvement of the photodegradation process. The possible mechanism of the photocatalytic activity of anodized ZrO$_2$ nanotubes is presented in Figure 12. Figure 12a,b shows the bg differences between tetragonal and monoclinic ZrO$_2$, respectively. Under light irradiation with energy higher than the bg, the photo-excited electrons can follow three possible paths. The first path (shown as (1) in Figure 12c) is the conventional path from the valence band to the conduction band of the ZrO$_2$ semiconductor. This path considers the prepared nanotubes as an ideal semiconductor without defects or impurities. The second

path passes through several types of intra-gap states, situated at different levels (shown as (2) in Figure 12c). The third path consists of the interfacial charge transfer between T-ZrO$_2$ and M-ZrO$_2$. In the current case, all three paths are possible since our results showed structural defects, oxygen vacancies, and the co-existence of both crystalline phases.
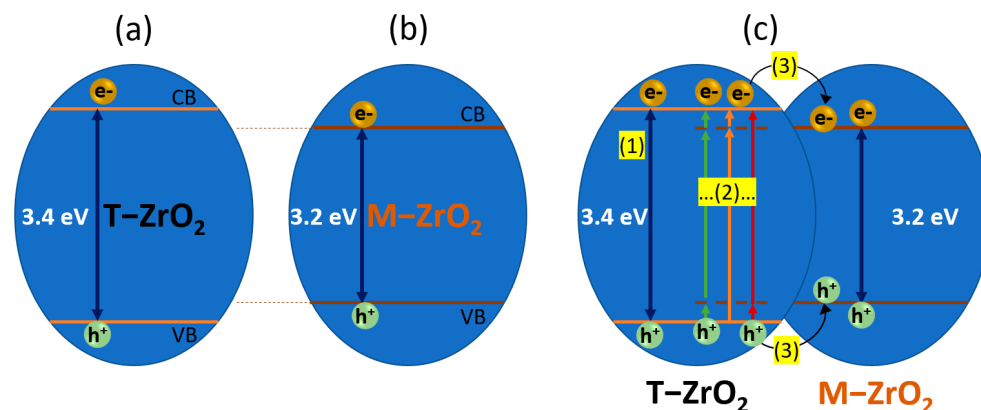

Figure 12. (**a**–**c**) The possible photocatalytic mechanism of ZrO2 nanotubes. (1), (2) and (3) are the possible photo-generated electron pathways (for more details, see text).

It has been reported that surface defects induced by low sample crystallinity serve as recombination centers for the photogenerated electron/hole pairs. However, the high crystallinity of the material promotes photocatalytic activity by transferring the photogenerated electrons from the bulk to the surface, leading to the inhibition of charge recombination and enhanced quantum efficiency [43,44]. The promoted charge separation, and, thus, the inhibited charge recombination, was witnessed by a decrease in the photoluminescence (PL), as shown in Figure 6. More work is needed to elucidate which mechanism is more probable after each annealing step at different temperatures.

2.5. Nanotube Stability and Scavenging Experiment

The stability of the prepared ZrO$_2$ NTs was carried out via XRD. The sample that was annealed at 400 °C was subjected to XRD before and after the photocatalytic BA degradation. Figure 13 shows diffractograms with peaks at similar positions before and after the degradation, using the NTs and showing their stability. Furthermore, the stability of the ZrO$_2$ NTs (400 °C) was tested after 5 consecutive degradation cycles of BA. The results showed stable performance after 5 cycles.
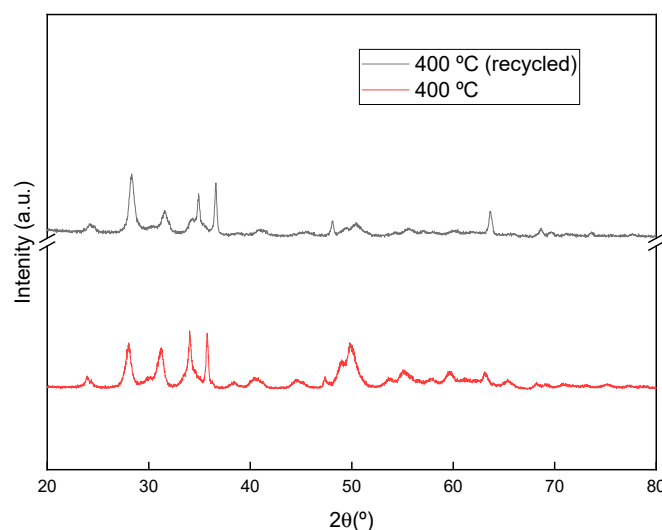

Figure 13. The XRD pattern of ZrO$_2$ NTs (400 °C) before and after BA photocatalytic degradation.

To elucidate the role of the ROS mediating BA degradation over ZrO_2 NTs (400 °C), different scavengers have been used. Quenching studies were performed using 1 mM of benzoquinone (BQ) as an effective scavenger for $O_2^{\bullet-}$, 1 mM of EDTA as a hole scavenger, and 20 mM of isopropyl alcohol as an $^{\bullet}OH$ scavenger. Each of the individual scavengers' experiments was carried out separately. After adding EDTA, the photodegradation of AB was reduced by 40%, suggesting the dominant contribution of the photogenerated holes in BA degradation. Conversely, the addition of isopropanol reduced the photocatalytic efficiency by 31%, testifying to the considerable contribution of the $^{\bullet}OH$ radicals in BA degradation. However, adding benzoquinone (BQ) slightly reduced the photocatalytic efficiency of ZrO_2 NTs, suggesting the weak contribution of the $O_2^{\bullet-}$. More work is needed to identify the photo-generated ROS at the interface of ZrO_2 NTs using advanced technologies.

3. Experimental

3.1. Anodic Formation Process of ZrO_2

Zirconia NTs were prepared by anodizing zirconium foil in an electrolytic bath containing 140 mL of ethylene glycol 98% (1:1), 2 mL of ammonium fluoride (NH_4F), and 6 mL of ultrapure water. All used reagents were of technical grade. The process was carried out at a constant voltage of 40 V for 60 min at room temperature under continuous magnetic stirring. After anodization, the samples were rinsed in ultrapure water to remove debris and occluded ions under ultrasound for 1 or 2 min and then dried in air. The zirconium and platinum electrodes were the anode and the cathode, respectively, and the distance between the two electrodes was maintained at 2 cm. The obtained samples were amorphous. The crystallization was carried out at different temperatures (400, 550, and 700 ° C) for 3 h with a heating rate of 5 °C/min in air.

3.2. Characterization of ZrO_2 NTs

Field-emission scanning electron microscopy (FE-SEM) and energy-dispersive X-ray spectroscopy (EDS) were used to characterize the morphology of the achieved ZrO_2 NTs. TEM images were carried out using a JEM-100CX2 transmission electron microscope (78290 Croissy-sur-Seine, France). TEM images were obtained by scraping off the oxidized layers from the substrates and dispersing them in ethanol while applying ultrasonic vibration.

The crystalline structure of the ZrO_2 NTs was characterized by XRD using the Rigaku Ultima IV diffractometer (Austin, TX 78717 USA) in the Bragg–Brentano configuration and Cu-Kα radiation (λ = 1.54060 Å). VESTA (version 3; Tsukuba-shi, Ibaraki 305-0005, Japan) was used as a 3D visualization system for the crystallographic study of the ZrO_2 phases and electronic state calculations. The spectral absorption of the ZrO_2 NTs samples was performed using a ultraviolet–visible–infrared spectrometer. The photoluminescence (PL) signals of ZrO_2 NTs were recorded using a fluorescence spectrophotometer (Perkin Elmer LS55; Waltham, MA 02451 USA) at an excitation wavelength of λ = 270 nm.

The photocatalytic performance of the ZrO_2 NTs was evaluated throughout the degradation of Black Amido (BA), a commercial dye diluted in an aqueous solution. A known mass of the prepared catalysts was placed in a beaker containing BA aqueous solution and was kept in the dark for 15 min to establish the adsorption-desorption equilibrium, succeeded by irradiation under UV. The used UV lamp is an OSRAM lamp with a power of 15 W.

4. Conclusions

We have successfully synthesized ZrO_2-NTs using the electrochemical method and studied the effect of annealing temperature on their structural, optical, and photocatalytic properties. Due to mechanical stress, the nanotubes collapsed and were destroyed at high annealing temperatures. The tetragonal and monoclinic phases coexisted for all annealed samples with different proportions. We noticed that an increase in annealing temperature reduced the tetragonal phase and increased the bandgap. This latter observation was attributed to the evaporation of the potential impurities introduced by the anodization

process and the evolution of the oxygen vacancies, as shown by the PL emission spectra. Crystalline phases play an important role in photocatalytic activity because of their chemical surface properties. In this work, we found that ZrO_2 NTs that were annealed at 400 °C exhibited the fastest photocatalytic performance. The scavenging experiments reduced photocatalytic activity by 40% when quenching the photogenerated holes, by 31 % after quenching $^{\bullet}OH$ radicals, and by only 12% when scavenging $O_2{}^{\bullet-}$. Further work is needed to understand the direct relationship between the preparation method, surface chemistry, and reactivity of such nanotubes for advanced applications.

References

1. Rtimi, S.; Sanjines, R.; Pulgarin, C.; Houas, A.; Lavanchy, J.-C.; Kiwi, J. Coupling of narrow and wide band-gap semiconductors on uniform films active in bacterial disinfection under low intensity visible light: Implications of the interfacial charge transfer (IFCT). *J. Hazard. Mater.* **2013**, *260*, 860–868. [CrossRef] [PubMed]

2. Hu, Z.; Lin, Z.; Su, J.; Zhang, J.; Chang, J.; Hao, Y. A Review on Energy Band-Gap Engineering for Perovskite Photovoltaics. *Sol. RRL* **2019**, *3*, 1900304. [CrossRef]

3. Zalnezhad, E.; Hamouda, A.M.S.; Jaworski, J.; Kim, Y.D. From Zirconium Nanograins to Zirconia Nanoneedles. *Sci. Rep.* **2016**, *6*, 33282. [CrossRef] [PubMed]

4. Garcia, J.C.; Scolfaro, L.M.R.; Lino, A.T.; Freire, V.N.; Farias, G.A.; Silva, C.C.; Leite Alves, H.W.; Rodrigues, S.C.P.; da Silva, E.F., Jr. Structucal, Electronic, and optical properties of ZrO_2 from Ab initio calculations. *J. Appl. Phys.* **2006**, *100*, 104103. [CrossRef]

5. Vacandio, F.; Eyraud, M.; Chassigneux, C.; Knauth, P.; Djenizian, T. Electrochemical synthesis and characterisation of zirconia nanotubes grown from Zr thin films. *J. Electrochem. Soc.* **2010**, *157*, 279–283. [CrossRef]

6. Wierzbicka, E.; Syrek, K.; Sulka, G.D.; Pisarek, M.; Janik-Czachor, M. The effect of foil purity on morphology of anodized nanoporous ZrO_2. *Appl. Surf. Sci.* **2016**, *388*, 799–804. [CrossRef]

7. Buica, G.-O.; Stoian, A.B.; Manole, C.; Demetrescu, I.; Pirvu, C. Zr/ZrO_2 nanotube electrode for detection of heavy metal ions. *Electrochem. Commun.* **2019**, *110*, 106614. [CrossRef]

8. Padovini, D.S.S.; Pontes, D.S.L.; Dalmaschio, C.J.; Pontes, F.M.; Longo, E. Facile synthesis and characterization of ZrO_2 nanoparticles prepared by the AOP/hydrothermal route. *R. Soc. Chem.* **2014**, *4*, 38484–38490. [CrossRef]

9. Rao, M.; Torabi, A.; Varghese, O.K. Anodically grown functional oxide nanotubes and applications. *MRS Commun.* **2016**, *6*, 375–396. [CrossRef]

10. Stępień, M.; Handzlik, P.; Fitzner, K. Synthesis of ZrO_2 nanotubes in inorganic and organic electrolytes by anodic oxidation of zirconium. *J. Solid State Electrochem.* **2014**, *18*, 3081–3090. [CrossRef]

11. Rtimi, S.; Pulgarin, C.; Sanjines, R.; Kiwi, J. Accelerated self-cleaning by Cu promoted semiconductor binary-oxides under low intensity sunlight irradiation. *Appl. Catal. B Environ.* **2016**, *180*, 648–655. [CrossRef]

12. Muratore, F.; Baron-Wiechéc, A.; Hashimoto, T.; Gholinia, A.; Skeldon, P.; Thompson, G. Growth of nanotubes on zirconium in glycerol/fluoride electrolytes. *Electrochim. Acta* **2011**, *56*, 10500–10506. [CrossRef]

13. Rtimi, S.; Pulgarin, C.; Bensimon, M.; Kiwi, J. New evidence for Cu-decorated binary-oxides mediating bacterial inactivation/mineralization in aerobic media. *Colloids Surf. B Biointerfaces* **2016**, *144*, 222–228. [CrossRef] [PubMed]

14. Zhang, L.; Han, Y. Enhanced bioactivity of self-organized ZrO_2 nanotube layer by annealing and UV irradiation. *Mater. Sci. Eng. C* **2011**, *31*, 1104–1110. [CrossRef]

15. Imparato, C.; Fantauzzi, M.; Passiu, C.; Rea, I.; Ricca, C.; Aschauer, U.; Sannino, F.; D'Errico, G.; De Stefano, L.; Rossi, A.; et al. Unraveling the Charge State of Oxygen Vacancies in ZrO_{2-x} on the Basis of Synergistic Computational and Experimental Evidence. *J. Phys. Chem. C* **2019**, *123*, 11581–11590. [CrossRef]

16. Chen, Q.; Yang, W.; Zhu, J.; Fu, L.; Li, D.; Zhou, L. In situ fluorine doped ZrO2-x nanotubes for efficient visible light photocata-lytic activity. *J. Mater. Sci. Mater. Electron.* **2019**, *30*, 701–710. [CrossRef]

17. Carvalho, J.M.; Rodrigues, L.C.; Felinto, M.C.; Nunes, L.A.; Hölsä, J.; Brito, H.F. Structure–property relationship of luminescent zirconia nanomaterials obtained by sol–gel method. *J. Mater. Sci.* **2015**, *50*, 873–881. [CrossRef]

18. Jouili, M. Caractérisations mécaniques et microstructurales des films de zircone obtenus par MOCVD et Sol-Gel. *HAL.* 2012. Available online: https://theses.hal.science/tel-00684387 (accessed on 2 April 2012).

19. Tsuchiya, H.; Schmuki, P. Thick self-organized porous zirconium oxide formed in H_2SO_4/NH_4F electrolytes. *Electrochem. Istry Commun.* **2004**, *6*, 1131–1134. [CrossRef]

20. Zhao, J.; Xu, R.; Wang, X.; Li, Y. In situ synthesis of zirconia nanotube crystallines by direct anodization. *Corros. Sci.* **2008**, *50*, 1593–1597. [CrossRef]

21. Lee, W.-J.; Smyrl, W.H. Zirconium Oxide Nanotubes Synthesized via Direct Electrochemical Anodization. *Electrochem. Solidstate Lett.* **2005**, *8*, B7–B9. [CrossRef]

22. Jiang, W.; He, J.; Zhong, J.; Lu, J.; Yuan, S.; Liang, B. Preparation and photocatalytic performance of ZrO_2 nanotubes fabricated with anodization process. *Appl. Surf. Sci.* **2014**, *307*, 407–413. [CrossRef]

23. Hahn, R.; Berger, S.; Schmuki, P. Bright visible luminescence of self-organized ZrO_2 nanotubes. *J. Solid State Electrochem.* **2008**, *14*, 285–288. [CrossRef]

24. Yang, W.; Li, D.; Li, L.; Huang, Y. Effect of anodizing temperature on the morphology and properties of ZrO_2 nanotubes. *Ceram. Int.* **2019**, *45*, 14306–14311.

25. Guo, L.; Zhao, J.; Wang, X.; Xu, X.; Liu, H.; Li, Y. Structure and Bioactivity of Zirconia Nanotube Arrays Fabricated by Anodization. *Int. J. Appl. Ceram. Technol.* **2009**, *6*, 636–641. [CrossRef]

26. Fang, D.; Huang, K.; Luo, Z.; Wang, Y.; Liu, S.; Zhang, Q. Freestanding ZrO_2 nanotube membranes made by anodic oxidation and effect of heat treatment on their morphology and crystalline structure. *J. Mater. Chem.* **2011**, *21*, 4989–4994. [CrossRef]

27. Yu, J.; Kiwi, J.; Wang, T.; Pulgarin, C.; Rtimi, S. Evidence for a dual mechanism in the TiO_2/Cu_xO photocatalyst during the degradation of sulfamethazine under solar or visible light: Critical issues. *J. Photochem. Photobio. A Chem* **2019**, *375*, 270–279. [CrossRef]

28. Wang, C.M.; Azad, S.; Thevuthasan, S.; Shuttanandan, V.; McCready, D.E.; Peden, C.H.F. Distortion of the Oxygen Sub-lattice in Pure Cubic ZrO_2, *J. Mater Res.* **2004**, *19*, 1315–1319. [CrossRef]

29. Moulzolf, S.C.; Yu, Y.; Frankel, D.J.; Lad, R.J. Properties of ZrO_2 Films on Sapphire Prepared by Zyclotron Resonance Sputtering. *J. Vac. Sci. Technol.* **1997**, *15*, 1211–1215. [CrossRef]

30. Yeh, S.-W.; Hsieh, T.-Y.; Huang, H.-L.; Gan, D.; Shen, P. Annealing induced oxidation and transformation of Zr thin film prepared by ion beam sputtering deposition. *Mater. Sci. Eng. A* **2007**, *452–453*, 313–320. [CrossRef]

31. Guinier, A. *Théorie et Technique de la Radiocristallographie*; Dunod: Paris, France, 1964.

32. Djurado, E.; Bouvier, P.; Lucazeau, G. Crystallite Size Effect on the Tetragonal-Monoclinic Transition of Undoped Nano-crystalline Zirconia Studied by XRD and Raman Spectrometry. *J. Solid State Chem.* **2000**, *149*, 399–407. [CrossRef]

33. Gravereau, G. Introduction à la Pratique de la Diffraction des Rayons X par les Poudres, Professeur. Université de Bordeaux 1, Talence, France, 2012.

34. Wang, Z.; Yang, B.; Fu, Z.; Dong, W.; Yang, Y.; Liu, W. UV–blue photoluminescence from ZrO_2 nanopowders prepared via glycine nitrate process. *Appl. Phys. A* **2005**, *81*, 691–694. [CrossRef]

35. Salah, N.; Habib, S.S.; Khan, Z.H.; Djouider, F. Thermoluminescence and photoluminescence of ZrO_2 nanoparticles. *Radiat. Phys. Chem.* **2011**, *80*, 923–928. [CrossRef]

36. Abidi, M.; Hajjaji, A.; Bouzaza, A.; Trablesi, K.; Makhlouf, H.; Rtimi, S.; Assadi, A.A.; Bessais, B. Simultaneous removal of bac-teria and volatile organic compounds on Cu_2O-NPs decorated TiO_2 nanotubes: Competition effect and kinetic studies. *J. Photochem. Photobiol. A Chem.* **2020**, *400*, 112722. [CrossRef]

37. Harrison, D.E.; Melamed, N.T.; Subbarao, E.C. A New Family of Self-Activated Phosphors. *J. Electrochem. Soc.* **1963**, *110*, 23–28. [CrossRef]

38. Méndez-López, A.; Zelaya-Ángel, O.; Toledano-Ayala, M.; Torres-Pacheco, I.; Pérez-Robles, J.; Acosta-Silva, Y. The Influence of Annealing Temperature on the Structural and Optical Properties of ZrO_2 Thin Films and How Affects the Hydrophilicity. *Crystals* **2020**, *10*, 454. [CrossRef]

39. Basahel, S.N.; Ali, T.; Mokhtar, M.T.; Narasimharao, K. Influence of crystal structure of nanosized ZrO_2 on photocatalytic degradation of methyl orange. *Nanoscale Res. Lett.* **2015**, *10*, 73. [CrossRef] [PubMed]

40. Kashyap, J.; Ashraf, S.M.; Riaz, U. Highly Efficient Photocatalytic Degradation of Amido Black 10B Dye Using Polycarbazole-Decorated TiO_2 Nanohybrids. *ACS Omega* **2017**, *2*, 8354–8365. [CrossRef]

41. Perillo, P.M.; Rodríguez, D.F. Anodization growth of self-organized ZrO_2 nanotubes on zircaloy-4. Evaluation of the photocatalytic activity. *Matéria* **2015**, *20*, 627–635. [CrossRef]

42. Reddy, C.V.; Babu, B.; Reddy, I.N.; Shim, J. Synthesis and characterization of pure tetragonal ZrO_2 nanoparticles with enhanced photocatalytic activity. *Ceram. Int.* **2018**, *44*, 6940–6948. [CrossRef]

43. Cao, Q.; Che, R.; Chen, N. Scalable synthesis of Cu_2S double-superlattice nanoparticle systems with enhanced UV/visible-light-driven pho-tocatalytic activity. *Appl. Catal. B Environ.* **2015**, *162*, 187–195. [CrossRef]
44. Cao, Q.; Li, Q.; Pi, Z.; Zhang, J.; Sun, L.-W.; Xu, J.; Cao, Y.; Cheng, J.; Bian, Y. Metal–Organic-Framework-Derived Ball-Flower-like Porous Co_3O_4/Fe_2O_3 Heterostructure with Enhanced Visible-Light-Driven Photocatalytic Activity. *Nanomaterials* **2022**, *12*, 904. [CrossRef] [PubMed]